

Programmable synthetic magnetism and chiral edge states in nano-optomechanical quantum Hall networks

Received: 27 March 2025

Jesse J. Slim ^{1,2}, Javier del Pino ^{3,4} & Ewold Verhagen ¹ 

Accepted: 24 July 2025

Published online: 12 August 2025

 Check for updates

Artificial magnetic fields break time-reversal symmetry in engineered materials –also known as metamaterials, enabling robust, topological transport of neutral excitations, much like edge channels facilitate electronic conduction in the integer quantum Hall effect. We experimentally demonstrate the emergence of quantum-Hall-like chiral edge states in optomechanical resonator networks. Synthetic magnetic fields for phononic excitations are induced through laser drives, while cavity optomechanical control allows full reconfigurability of the effective metamaterial response of the networks, including programming of magnetic fluxes in multiple resonator plaquettes. By tuning the interplay between network connectivity and magnetic fields, we demonstrate both flux-sensitive and flux-insensitive localized mechanical states. Scaling up the system creates spectral features that are precursors to Hofstadter butterfly spectra. Site-resolved spectroscopy reveals edge-bulk separation, with stationary phononic distributions signaling chiral edge modes. We directly probe those edge modes in transport measurements to demonstrate a unidirectional acoustic channel. This work unlocks new ways of controlling topological phononic phases at the nanoscale with applications in noise management and information processing.

The discovery of the integer quantum Hall effect (IQHE) in a two-dimensional electron gas under a magnetic field¹ sparked significant interest in new phases of matter with unique properties. As formalized by Thouless et al.², the quantized Hall conductance in the IQHE is connected to a nontrivial topology of the bulk wavefunctions in momentum space. It emerges as the magnetic field breaks time-reversal (T) symmetry, so that the electron's wavefunction acquires a nonreciprocal Aharonov-Bohm (AB) phase³ when traversing the magnetic vector potential. Interference from waves following multiple paths then creates an insulating bulk and chiral (one-way) conducting edge states, robust against backscattering and protected by the bulk's topology rather than microscopic details^{2,4}.

As the IQHE is essentially a wave phenomenon⁵, it was realized that it equally applies to classical waves^{6,7}. The unique properties of the resulting *bosonic* topological phases of matter incited considerable fundamental and technological interest in photonic and phononic settings^{8,9}. While theoretical proposals for topological phases with broken time-reversal symmetry in *nanomechanical systems* have been put forward, no experimental realizations exist to date⁹. To induce AB phases for such neutral excitations requires complex engineering to break T -symmetry and mimic the effect of a magnetic field, without relying on charge. For electromagnetic waves, this is for example achieved with magneto-optical materials^{10–12} and for low-frequency sound through rotating fluids or coupled gyroscopes^{13,14}. The materials and system limitations involved in these approaches make scaling to

¹Center for Nanophotonics, AMOLF, Amsterdam, The Netherlands. ²Australian Research Council Centre of Excellence for Engineered Quantum Systems (EQUS), School of Mathematics and Physics, University of Queensland, St Lucia, QLD, Australia. ³Department of Physics, University of Konstanz, Konstanz, Germany. ⁴Departamento de Física Teórica de la Materia Condensada and Condensed Matter Physics Center (IFIMAC), Universidad Autónoma de Madrid, Madrid, Spain. ✉e-mail: verhagen@amolf.nl

the nanophotonic and nanomechanical domain a significant challenge. Moreover, they generally lack in situ active tunability.

Dynamical modulation offers a powerful alternative to break T -symmetry. Using time-varying parametric drives, gauge fields for light and sound can be engineered—and reconfigured—at will^{15–20}. In these Floquet systems, harmonic modulation of the coupling between bosonic resonators with distinct resonance frequencies enables frequency conversion, inducing a hopping (beam-splitter) interaction between them. The modulation phase is imprinted on the transferred excitations, and the process is nonreciprocal: exchanging the initial and target resonators results in a phase pickup of opposite sign, analogous to the Peierls phase for an electron traveling in a magnetic vector potential. After connecting resonators in a loop, such nonreciprocal hopping phases allow the creation of an AB loop phase that corresponds to a T -breaking synthetic magnetic flux piercing the loop. In a single loop, AB interference enables controllable nonreciprocal transmission. In extended lattices, combining many Aharonov-Bohm loops across all unit cells, such as in Fig. 1a, mimics a homogeneous magnetic field and enables synthetic quantum Hall phases^{15,20–25}.

Implementing these ideas in the nanomechanical domain has so far remained elusive. Multimode cavity optomechanical systems constitute a promising route to do so, naturally providing time-varying potentials for light and sound that can induce frequency-converting nonreciprocal couplings and provide T -breaking gauge fields^{26–32}. It was envisioned that topological phases for sound and light could be implemented in optomechanical lattices, specifically Chern insulators akin to the IQHE^{33,34}. While those first proposals relied on the resolved-sideband limit, requiring precise tuning of many high- Q photonic resonators, recently, time-modulated lower- Q cavities have offered a flexible alternative to imprint gauge fields for MHz frequency nanomechanical resonators^{32,35–37}. While optomechanical couplings have been used to map (T -symmetric) mechanical topological states using optical modes³⁸ and microwave topological states using mechanical

resonators³⁹, the realization of a Chern insulator that breaks T -symmetry through optomechanical driving has remained an outstanding challenge.

In this work, we bring quantum Hall physics into the nanomechanical domain using a versatile optomechanical platform that exploits multiple nanomechanical modes in a ‘synthetic dimension’. Optical driving fully controls the coupling strength *and* phase between each pair of resonators. The coherent hopping phase is nonreciprocal, unlike a trivial reciprocal phase that could be established through retardation. This control enables the creation of arbitrary resonator networks with broken T -symmetry that feature multiple AB loops (‘plaquettes’) with individually tunable synthetic magnetic fluxes. We implement increasingly complex networks to study the role of artificial magnetic fluxes in multi-plaquette systems. We find that the relative handedness of neighboring plaquettes significantly impacts dynamics, and controls the symmetries and localization of mechanical states within the network. Finally, in a four-plaquette lattice, we launch and track a chiral edge mode that witnesses the emergence of the IQHE in a minimal nanomechanical network. This provides an essential advance in the pursuit to realize topological phases of sound induced by light³³.

Unlike most experimental approaches to topological bosonics^{8,9}, the platform we use provides full, active, control over each individual interaction strength and phase in the network. This means that in a single experimental system, any network Hamiltonian can be ‘programmed’ at will, and the resultant response can subsequently be probed using either coherent or thermal drives. Our work opens the ability to study the physical and technological implications of complex networks with broken time-reversal symmetry and the associated topological phases of matter. Doing so in the nanomechanical domain is particularly interesting due to the importance of nanomechanical resonators in sensing applications, quantum and classical information processing, and on-chip control of thermal fluctuations.

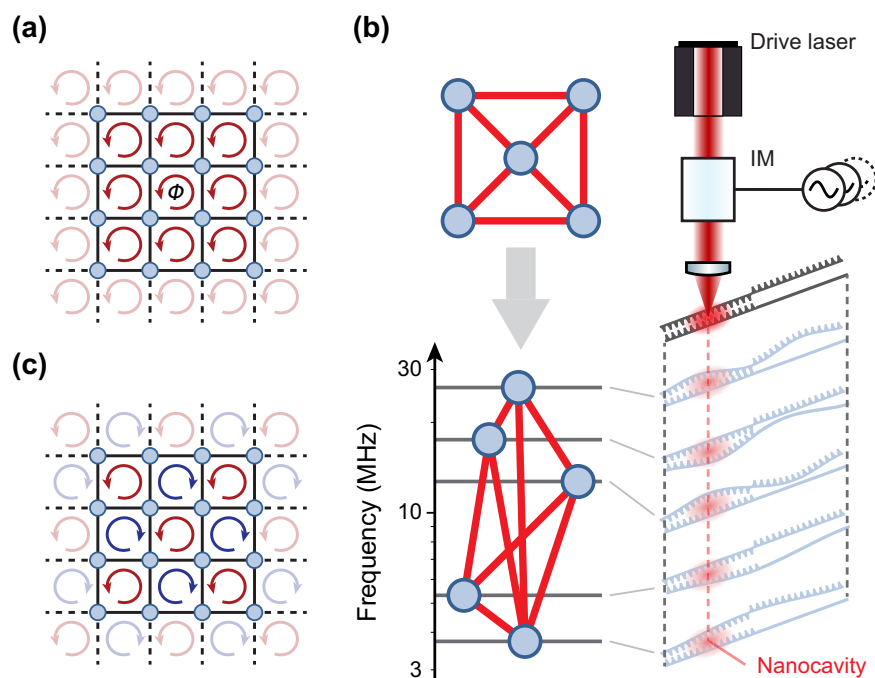


Fig. 1 | Constructing resonator networks with controllable synthetic magnetic fields. **a** Square lattice threaded by a uniform magnetic flux Φ per plaquette, inducing counterclockwise chirality (arrow). A small section is highlighted for clarity. **b** Resonator graph with 5 resonators connected by 8 hopping interactions. Resonators represent mechanical overtones of a nano-optomechanical cavity,

which span a synthetic frequency dimension. Each interaction is generated by modulating the optical drive at a mechanical difference frequency, establishing full connectivity by superposing (incommensurate) modulation tones. **c** Control over each coupling phase allows for creating lattices with highly inhomogeneous magnetic fields, difficult to achieve in natural materials.

Results

Programmable network Hamiltonians with Aharonov-Bohm phases

The employed device, described in more detail in^{35,37}, consists of a sliced photonic crystal nanobeam⁴⁰ and is shown in Fig. 1b. It supports multiple non-degenerate mechanical modes with frequencies Ω_j ranging from 3.7 MHz to 26 MHz, each dispersively coupled to the optical field of a telecom-wavelength nanocavity (linewidth $\kappa/(2\pi) = 320$ GHz). The optical resonance frequency shifts by $\sum g_{0,j}x_j$, where $g_{0,j}$ is the vacuum optomechanical coupling rate of mode j and x_j its displacement in units of its zero-point motion amplitude $x_{zpf,j}$. Operating in the unresolved sideband regime ($\Omega_j \ll \kappa$), the cavity enables optical read-out of both thermal and driven mechanical motion, as displacements x_j modulate the reflected intensity of a detuned probe laser. This reveals five optically active mechanical resonances in the thermomechanical spectrum, with linewidths $\gamma_j/(2\pi) \approx 1 - 7$ kHz and coupling rates $g_{0,j}/(2\pi) \approx 2 - 6$ MHz (see Supplementary Table 1).

The cavity is also illuminated with a drive laser detuned from the cavity resonance frequency by $\Delta = \kappa/(2\sqrt{3})$ to induce a strong optomechanical spring effect through radiation pressure back-action. Modulating its intensity at the frequency difference $\Omega_j - \Omega_k$ between modes (henceforth, called resonators) j and k creates an effective mechanical beamsplitter interaction, at a rate $J_{jk} = c_{jk}^m \bar{n}_c \sqrt{3g_{0,j}g_{0,k}}/(2\kappa) = J_{kj}$, where \bar{n}_c and c_{jk}^m is the average cavity photon population and modulation depth, respectively. Crucially, each modulation tone's phase offset imprints a phase shift φ_{jk} on the interaction, akin to the Peierls phase imprinted by a magnetic vector potential on electron hopping³².

We can establish multiple mechanical couplings simultaneously, by superposing the necessary modulation tones on the single detuned drive laser. Here we emphasize that it is important in our experiments that the mechanical spectrum is irregular, i.e., that all mechanical frequency differences in the system are incommensurate (to a precision given by the mechanical linewidth). This ensures that the amplitude and phase of each transition can be addressed by a specific modulation tone. Moreover, this means that unwanted parametric interactions due to frequency mixing can be avoided. The resulting temporal modulation of the optomechanical spring effect thus allows programming the effective Hamiltonian of a resonator network through modulation depths and phases of the various modulation tones, coupling the mechanical modes forming the nodes of the network in the synthetic frequency dimension through frequency-converting interactions. Precise tuning of the modulation tones to the difference frequencies can also eliminate all on-site energies. The Hamiltonian for N resonators, in terms of the resonator annihilation operators a_j in frames rotating at Ω_j , then reads

$$H = \sum_{j,k=1}^{N,N} J_{jk} e^{-i\varphi_{jk}} a_j^\dagger a_k, \quad \varphi_{kj} = -\varphi_{jk}. \quad (1)$$

Hamiltonian (1) conserves phonon number and exhibits a $U(1)$ gauge symmetry, where gauge transformations $a_j \rightarrow a_j e^{i\delta_j}$ correspond to shifts in the time origin that modify the coupling phases φ_{jk} . However, the presence of closed loops ('plaquettes') in the system crucially allows for AB interference, giving rise to a finite, gauge-invariant flux $\Phi_p = \sum_{j,k \in p} \varphi_{jk}$ for each plaquette p . In addition to the coherent dynamics governed by Eq. (1), each resonator is coupled to an independent thermal bath with an occupation of $n_j \sim 10^6$, leading to thermal fluctuations and dissipation at a rate γ_j . We routinely achieve coupling strengths J_{jk} that exceed dissipation, i.e., $J_{jk} > \gamma_j, \gamma_k$, bringing the system into the strong mechanical coupling regime.

Similar to the adjacency matrix that encodes network connectivity⁴¹ or the impedance matrix that governs current flow in circuits⁴², the matrix \mathbf{J} that encodes the complex elements $J_{jk} e^{-i\varphi_{jk}}$ in Eq. (1) captures the strength and phase of all couplings between

resonators. Each non-zero entry in \mathbf{J} thus defines the mechanical network layout. In the experiment, adjusting the amplitudes and phases of the modulation tones allows independent control over each matrix element, while deterministic phase relations are obtained by referencing all tones to a common clock (see ref. 35). This control makes it possible to engineer \mathbf{J} to mimic complex coupling geometries (e.g., lattices or complete graphs) threaded by synthetic fluxes of arbitrary complexity, including highly inhomogeneous magnetic fields as exemplified in Fig. 1c.

The simplest closed-loop network is a single plaquette, coupled by equal rates $J_{jk} = J$ and threaded by a flux $\Phi = \varphi_{12} + \varphi_{23} + \dots + \varphi_{M1}$. Here, AB interference shifts the eigenfrequencies,

$$\epsilon_k = 2J \cos\left(\frac{2\pi k + \Phi}{N}\right), \quad (2)$$

of its momentum eigenmodes, labeled by k ,

$$\tilde{a}_k = \frac{1}{\sqrt{N}} \sum_{j=1}^N e^{-i2\pi k j/N} a_j, \quad (3)$$

expressed in the gauge where Φ is evenly distributed across links ($\varphi_{12} = \varphi_{23} = \dots = \varphi_{M1} = \Phi/N$). For multi-plaquette networks, we later apply Eq. (3) in a generalized sense where the label j traverses only the outer nodes. Any flux $\Phi \neq 0, \pi$ breaks T -symmetry, lifting the degeneracy between the eigenmodes \tilde{a}_k – which exhibit a chiral phase advance between resonators of $2\pi k/N$. In prior experiments with $N=3$, where $k = \{-1, 0, 1\}$, we observed that interference between the \tilde{a}_k states produced clockwise (counterclockwise) chiral Rabi oscillations for $\Phi = \pi/2$ ($\Phi = -\pi/2$) in the time evolution³⁵.

Interference with multiple magnetic flux plaquettes

Crucially, the collective phenomena in larger lattices pierced by magnetic fluxes originate from the interference of excitations on *multiple* plaquettes in the lattice. For example, in the Harper-Hofstadter model⁴³ interference between adjacent plaquettes leads to the insulating bulk and localization of chiral states on the edge of a network that are characteristic of the IQHE. We study such emergent behavior by constructing nano-optomechanical networks containing multiple flux plaquettes, leveraging the platform's reconfigurability. While flux tunes the eigenfrequencies ϵ_k (Eq. (2)) of a single AB loop with equal couplings J , its eigenstates remain evenly distributed for any Φ ($\langle a_j^\dagger a_j \rangle \equiv \text{const.}$). But as soon as a network contains more than one loop, interference between adjacent plaquettes leads to eigenstates with inhomogeneous distributions, controlled by flux. The four-mode 'diamond' network shown in Fig. 2a features two AB loops $a_4 - a_1 - a_3$ and $a_3 - a_2 - a_4$, fused along the central link $a_3 - a_4$ and pierced by independent fluxes. The relative handedness of the fluxes critically impacts the diamond's spectrum and the eigenstate localization.

With opposing flux chiralities $\Phi, -\Phi$, the phase vorticities for each loop align along the central link, and the net flux through the perimeter vanishes. We thus choose a gauge where both fluxes are sustained by the central link to simplify calculations. For equal perimeter couplings J , destructive interference then leads to an antisymmetric mode $\tilde{a}_{\text{apex}} = (a_1 - a_2)/\sqrt{2}$, localized solely on the apex resonators a_1, a_2 . The localization keeps \tilde{a}_{apex} unaffected by the central coupling rate J_c and frequency-insensitive to Φ . In Fig. 2b, the thermomechanical spectra (top) show mode \tilde{a}_{apex} as a flat band near zero detuning, exclusive to the apex resonators' sidebands. In this system, the apex localization, representing a compact localized state—where amplitude is confined to a few select sites—stems purely from geometry and remains robust under varying flux⁴⁴. However, the same coupling principle allows engineering nanomechanical 0- and π -flux rhombic chains in our platform, where localization arises from both geometry and Aharonov-Bohm interference, leading to "Aharonov-Bohm caging."^{45–49}

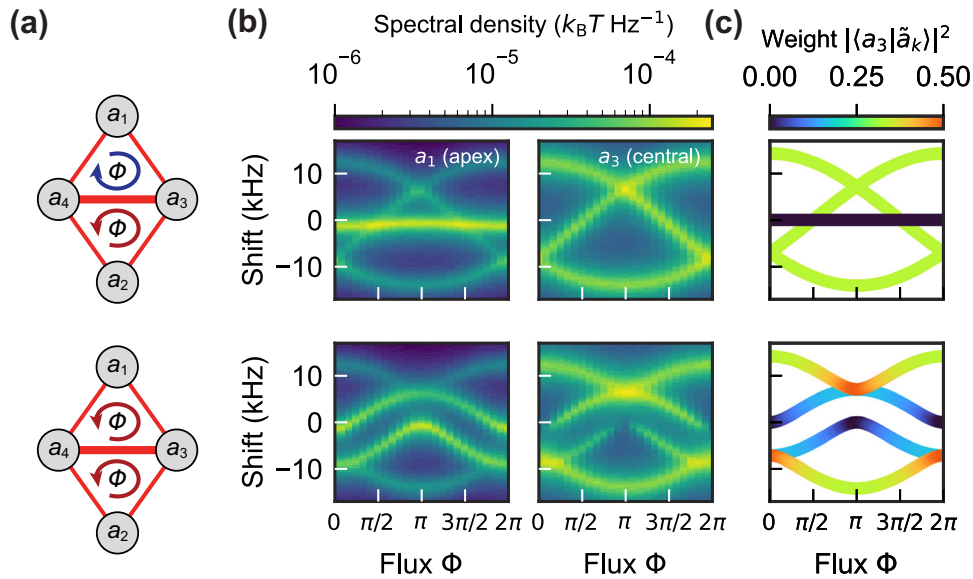


Fig. 2 | Interference between two adjacent plaquettes in a diamond configuration. **a** Four resonators a_j form a diamond configuration with two adjacent plaquettes, pierced by opposite fluxes Φ , $-\Phi$ (top) or equal fluxes Φ (bottom). The perimeter coupling rate is $J/(2\pi) = 5$ kHz, and the central link is coupled at $J_c = J/\sqrt{2}$. **b** Measured thermomechanical spectra around the frequency of the apex resonator a_1 (left) and central resonator a_3 (right) for varying flux Φ . The spectra for the other apex and central resonators are similar. In the diamond with opposite fluxes (top), eigenmodes with flux-independent localization emerge. One antisymmetric mode,

\tilde{a}_{apex} , is localized at the apex and remains unaffected by Φ , while the other modes are delocalized and tune like those of a three-mode plaquette with $J_c = J/\sqrt{2}$ (Methods). For equal-handed fluxes (bottom), all eigenmodes tune with flux, both in frequency and localization. The central link couples opposite momentum states, and at $\Phi = 0$ and $\Phi = \pi$, their superpositions localize entirely on either the apex or central resonators. **c** Weight of central resonator a_3 in each hybridized eigenmode \tilde{a}_k of the diamond. The weight of apex resonator a_1 , as shown in Supplementary Fig. 1a, is complementary.

The remaining three eigenmodes depend on both J_c and Φ , affecting their frequency and localization. However, when $J_c = J/\sqrt{2}$, all eigenstates become flux-independent, and are given by \tilde{a}_{apex} and

$$\tilde{a}_k = \left[(a_1 + a_2)/\sqrt{2} + e^{-i2\pi k/3} a_3 + e^{i2\pi k/3} a_4 \right] / \sqrt{3}, \quad (4)$$

with $k = \{-1, 0, 1\}$, which represent Fourier modes of an effective three-mode loop obtained by removing the uncoupled apex mode. Interestingly, \tilde{a}_k preserve the phase-chiral character of the two three-mode loops forming the diamond, with eigenfrequencies tuning exactly as those of a single three-mode loop, as shown in Fig. 2 (top) and detailed in Methods.

As Fig. 2 (bottom) shows, the situation is strikingly different when both plaquettes are threaded by equally handed fluxes Φ , Φ . Their vorticities along the central link are antiparallel, so that multi-loop interference causes *all* eigenstates to have flux-dependent weights. The perimeter is pierced by a net flux of 2Φ , which we can distribute evenly over its links. In the basis of eigenstates \tilde{a}_k of perimeter momentum $k = \{-1, 0, 1, 2\}$, given in Eq. (3), the hopping matrix—order $\{\tilde{a}_0, \tilde{a}_2, \tilde{a}_1, \tilde{a}_{-1}\}$ —becomes block-diagonal,

$$\mathbf{J} = \begin{bmatrix} \epsilon_0 + J_c/2 & -J_c/2 & 0 & 0 \\ -J_c/2 & \epsilon_2 + J_c/2 & 0 & 0 \\ 0 & 0 & \epsilon_1 - J_c/2 & J_c/2 \\ 0 & 0 & J_c/2 & \epsilon_{-1} - J_c/2 \end{bmatrix}, \quad (5)$$

where ϵ_k are given in Eq. (2) for flux $\Phi \rightarrow 2\Phi$. The central coupling J_c mixes the opposite momentum states $\tilde{a}_0 \leftrightarrow \tilde{a}_2$ and $\tilde{a}_1 \leftrightarrow \tilde{a}_{-1}$, which attain degenerate ϵ_k for $\Phi = 0, \pi$, respectively. Consequently, a spectral gap opens at those fluxes of width J_c (see “Methods” and Supplementary Fig. 2), where (anti)symmetric superpositions of opposite momentum states are formed. These localize excitations in the apex or central resonators, as observed in Fig. 2b and c, bottom, for the central site a_3 by disappearing sidebands at $\Phi = 0, \pi$, while the disappearance

of apex sidebands is masked at $J_c/J = \sqrt{2}$. Finally, at T -breaking fluxes $\Phi \neq 0, \pi$, the ϵ_k -degeneracies lift and all modes delocalize. Evidently, the equal-handed diamond no longer mimics its constituent loops.

Edge localization and integer quantum Hall physics

When moving to larger lattices with magnetic flux, interference between plaquettes plays an essential role in the emergence of the features associated with quantum Hall phases. In infinite periodic lattices, such as the square-lattice Harper-Hofstadter model, a constant magnetic field controls the fractal complexity in the spectrum known as the Hofstadter butterfly, related to the competition between the lattice length scale and the magnetic length⁴³. A larger lattice uncovers more of the butterfly’s details by accommodating a broader range of commensurate and incommensurate ratios (“Methods”). In a finite Hofstadter system, the characteristic chiral edge modes appear in the gaps of the butterfly spectrum, with energy localized on the outer edge of the lattice while the magnetic flux renders the bulk insulating. Similar effects are observed in other planar discretizations, including triangular, hexagonal Kagome lattices, and hyperbolic tilings^{50–54}.

The mechanisms at play can be observed in systems that contain even just five resonators. We construct the five-mode wheel graph W_5 (Fig. 3a), with four resonators a_j forming a ring (rates J) and connected to a central hub resonator a_1 (rates J_s). With oppositely handed fluxes through adjacent plaquettes (Fig. 3, top), the vorticities of neighboring plaquettes in W_5 align along their common links. This results in flux-insensitive antisymmetric eigenmodes, $(a_2 - a_4)/\sqrt{2}$ and $(a_3 - a_5)/\sqrt{2}$, similar to the diamond’s apex state. For equal couplings $J_s = J$, the remaining states behave like a three-mode loop with unequal couplings $J, J/\sqrt{2}$ (Fig. 3b, top; further details in Methods). Interestingly, at the special ratio $J_s/J = \sqrt{2}$, all states become flux-independent and delocalized, and the system acts as a fusion of its constituent loops.

A striking shift occurs with equally handed fluxes, where the thermomechanical spectrum reveals states confined to the perimeter and tunable with flux (Fig. 3, bottom). We will call these states “edge

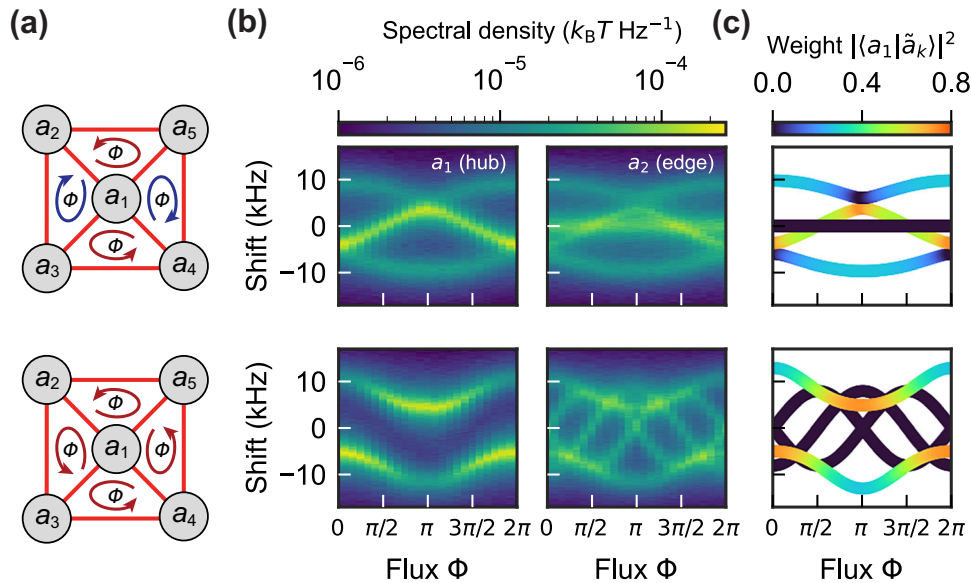


Fig. 3 | Multi-plaquette interference in a wheel graph. **a** Hub resonator a_1 is coupled to four perimeter resonators a_j in a wheel graph configuration with equal rates $J = J_s$. The wheel has four plaquettes pierced by either alternating fluxes $\Phi, -\Phi$ (top, $J/(2\pi) = 3$ kHz) or equal-handed fluxes Φ (bottom, $J/(2\pi) = 4$ kHz). **b** Thermo-mechanical spectrum of the hub a_1 (left) and perimeter a_2 (right) for varying flux Φ . With alternating fluxes, the spectrum mirrors the opposed-flux diamond, forming

two degenerate, flux-insensitive eigenmodes that decouple from the hub ($(a_2 - a_4)/\sqrt{2}$ and $(a_3 - a_5)/\sqrt{2}$), while the other three modes delocalize over all resonators. With equal fluxes, two modes delocalize across all resonators, and three phase-chiral modes localize on the perimeter. **c** Weight of hub resonator a_1 in each of the hybridized eigenmodes \tilde{a}_k of the wheel. The weight of edge resonator a_2 , as shown in Supplementary Fig. 1b, is complementary.

states” because of their confinement to the perimeter of this small lattice. Writing the Hamiltonian in the momentum basis of the edge states b_k according to Eq. (3) and choosing a gauge where the spokes carry no phase yields

$$H_{W_5, \odot} = J_s (a_1^\dagger b_0 + b_0^\dagger a_1) + \sum_{k=-1}^2 \epsilon_k b_k^\dagger b_k, \quad (6)$$

where ϵ_k are given by Eq. (2) for $N = 4$ and $\Phi \rightarrow 4\Phi$ (perimeter net flux). The spoke couplings J_s hybridize the hub state a_1 with the zero-momentum edge state b_0 , opening a spectral gap as observed in Fig. 3b and c, bottom. At $\Phi = \pm \pi/2$, only the edge state $b_{\pm 1}$ remains at zero detuning.

To study the character of the zero-detuning edge state experimentally, we construct ‘field maps’ of the distribution of mechanical amplitude over the nodes of the network. Figure 4a shows the recorded fluctuation amplitudes in the five network nodes, obtained by integrating the thermal fluctuations around the frequencies of each of the five resonators (between $\Omega_j \pm 2 \times 2\pi$ kHz). Maps are shown for both homogeneous fluxes $\Phi = \pi/2$ and $\Phi = -\pi/2$. As can be seen in Fig. 3b (bottom), this corresponds to mapping the excitation of the mid-gap edge state for positive and negative magnetic field, respectively. The field maps in Fig. 4a again show that these edge states are confined at the perimeter, with minimum amplitude at the hub node. The slight variation in amplitude among the different perimeter nodes can be explained by the variation in their damping rates and bath occupancies.

As the edge states are extended over the entire perimeter, their chiral nature is not revealed in this type of field map. We therefore perform a different type of measurements, probing the transport of coherent (continuous-wave) excitations of a single driven resonator. Figure 4b shows the response as a function of drive frequency in each of the five nodes, at \mathcal{T} -breaking flux $\Phi = \pm \pi/2$. Driving the hub resonator a_1 at $\Delta_m = 0$ fails to excite the edge state, but driving the perimeter resonator a_2 elicits a sharp response near $\Delta_m = 0$ across all perimeter resonators, with the hub’s response remaining

flat. Crucially, as there is a trade-off between coherent energy transfer through the network and dissipation at each site (see Supplementary Fig. 3), the amplitude is attenuated further away from the source, and the decaying amplitude reveals energy flow. The relative heights of the zero-detuning peaks thus indicate that the amplitudes decay along the edge with a clockwise or a counterclockwise direction (Fig. 4b), depending on the sign of the flux, revealing the chiral nature of the energy flow. In Fig. 4c (left), we show the measured field maps of the driven experiment; regrouping the edge amplitudes under resonant driving ($\Delta_m = 0$) for both signs of the flux. These experimental field maps explicitly show the reversal of chirality—a direct result of tunable time-reversal symmetry breaking. They capture small differences in amplitudes due to inhomogeneities in the network (i.e., the damping rates not being equal). Both the chirality and the detailed amplitude distributions of the experimentally mapped edge states correspond well to the theoretically obtained field maps in Fig. 4c (right).

We thus observe chiral transport along the perimeter of the W_5 network, enabled by AB interference between plaquettes. As the single hub site a_1 is shared among the four plaquettes that make up W_5 , destructive interference suppresses the excitation of a_1 as the edge wave propagates. These mechanisms ensure that the basic characteristics of the chiral edge states that exist in Chern insulators featuring the IQHE can be recognized in optomechanical networks, even if they are composed of a modest number of resonators. As such, the experiments reported in Figs. 3, 4 witness the emergence of the IQHE in small optomechanical lattices, including edge confinement, chiral transport, and destructive interference in the bulk. Indeed, this behavior of edge state formation due to interfering flux plaquettes is not unique to the specific W_5 network. In Supplementary Fig. 4, we show similar phenomenology in a network with three interfering plaquettes. In that same Supplementary Fig., we further emphasize the programmability of the networks by comparing to a specific example of inhomogeneous fluxes parametrized as $(0, -\Phi, \Phi + \pi)$. With that choice of fluxes, the network’s eigenmode localization is observed to tune strongly with the flux parameter Φ , while its eigenfrequencies are

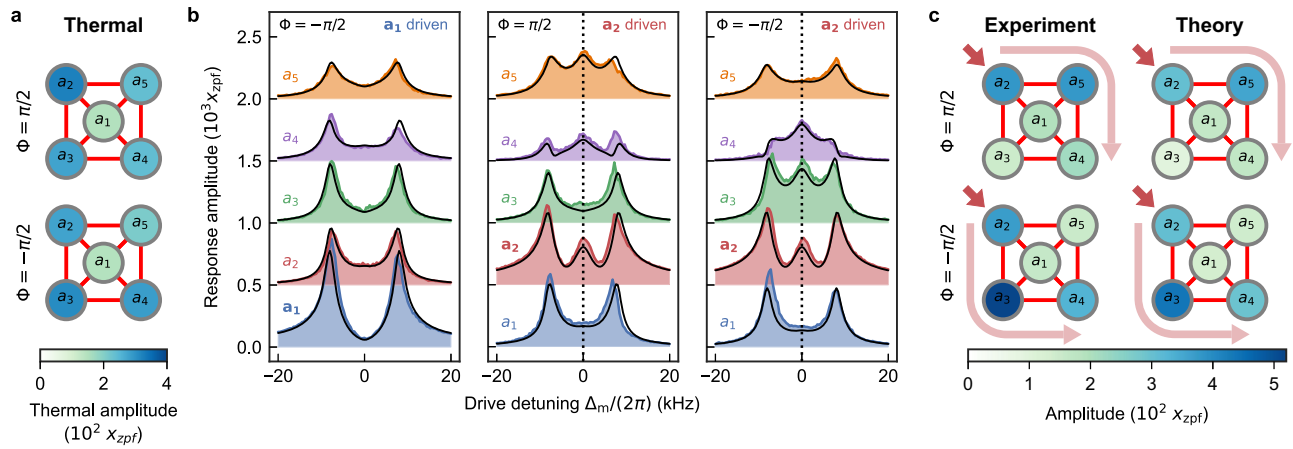


Fig. 4 | Field maps and transport along the perimeter of a wheel graph: observation of chiral edge states. **a** Field maps of thermal fluctuations in the W_5 network. These plot the root-mean-square thermomechanical amplitude of the zero-detuning mode for each resonator in the network (integrated between $\Omega_j \pm 2 \times 2\pi$ kHz), for homogeneous fluxes $\Phi = \pm \pi/2$. At these frequencies and fluxes, the edge states are mapped. **b** Amplitude response of the five-mode wheel network W_5 with equal-handed flux $\Phi = \pm \pi/2$ (Fig. 3, bottom) to continuous wave driving of the central resonator a_1 (left) and perimeter resonator a_2 (middle and right). Coupling rates $J/(2\pi) = J_c/(2\pi) = 4$ kHz. Driving the perimeter resonator a_2 excites the edge mode at zero detuning, while driving the hub resonator a_1 does not. Measured amplitudes are in good agreement with the predicted responses (black

lines, Methods), with all necessary parameters (coupling J , dissipation γ_j and driving strength f_j) determined independently. **c** Field maps of locally driven edge states: Amplitude response at each site of the network when resonantly driving a_2 ($\Delta_m = 0$, indicated by dotted lines in panel a). Clockwise (counter-clockwise) chiral transport along the perimeter is observed for $\Phi = \pi/2$ ($\Phi = -\pi/2$) from the decay away from the source, due to the trade-off between vibration transfer and decay at each site (see Supplementary Fig. 3). Differences in clockwise and counter-clockwise transport are explained by disorder in the dissipation rates (Supplementary Table 1). Experimental data is shown on the left, theoretical simulations of the driven experiments (including the measured dissipation rates) are shown on the right.

completely insensitive to Φ —in stark contrast to the quantum Hall behavior induced by uniform magnetic fields.

Discussion

Despite involving only a few interfering nanomechanical plaquettes, our experiments could capture core features of chiral edge states as they are known to exist in extended lattices with the IQHE. The connection of the above observations in the W_5 network to the IQHE in extended systems can be made more concrete in multiple ways. Indeed, the W_5 lattice could be extended to a larger lattice with topological band structure by continuously adding resonator nodes. For example, a square tiling of the W_5 graph (Fig. 5a) forms a so-called ‘Union Jack (UJ)’ lattice, a.k.a. tetrakis square tiling^{55,56}. This lattice forms a Chern insulator, featuring bands with opposite Chern numbers $C = \pm 1$ separated by a direct band gap, as shown in Fig. 5b and analysed in Methods. Boundaries of the UJ lattice under a uniform flux support chiral edge states that span the gap, as illustrated in the dispersion of a finite-width ribbon in Fig. 5c. The edge states, depicted in Fig. 5d for various different wavevectors, are localized near the edge, with the degree of localization determined by the spectral position of the state’s energy within the gap. Alternatively, the W_5 lattice could be extended to a triangular or square lattice with equal flux along each plaquette, which are also known Chern insulators with full topological band gaps.

A natural question is how the optomechanical platform we exploit can be expanded to employ larger numbers of modes, and thus more complex networks. First, we recognize that a larger number of physically separated beams could be used, thus expanding the system by adding one or two spatial lattice dimensions to the synthetic (frequency) mode dimension that we use here. In ref. 32, a two-dimensional resonator lattice of sliced photonic crystal nanobeams was envisioned, connected and programmed by using multiple optical cavities, which could be addressed from free space using a laser field that is shaped in a suitable fashion. Alternatively, multiple optomechanical resonators could be coupled through optical waveguides on the surface of a chip. In either case, to keep the number of control tones manageable, some of the mechanical modes in the network

could have equal frequencies, such that single modulation tones can address multiple connections in the network. Depending on the network one aims to create, this is not necessarily a problem: Indeed, only a finite set of independently tunable hopping phases is needed to implement the IQHE, due to gauge invariance²³. Second, we envision that even in a single optical cavity, many more mechanical modes could be coupled than we have demonstrated in this work. The physical phenomena we demonstrated here require coupling rates $|J_{jk}|$ to significantly exceed the mechanical linewidths γ_j, γ_k , i.e., strong mechanical coupling and normal mode splitting. Since $|J|$ is of the order of the maximal optical spring shift, the above requirement is equivalent to having the optomechanical cooperativity $C = 4g_0^2 \bar{n}_c / (\kappa \gamma)$ significantly exceed unity. This can be reached for a larger amount of mechanical modes by for example increasing the laser power, reducing the optical linewidth κ , or reducing the mechanical linewidth γ . The mechanical linewidth in the platform studied here would be reduced naturally by more than an order of magnitude by operating at cryogenic temperatures⁵⁷.

Importantly, many different optomechanical resonator systems across various scales and materials reach the regime of large cooperativity⁵⁸, and one can thus imagine the use of optomechanical lattices in systems that naturally feature many mechanical modes, such as membranes with phononic hole arrays⁵⁹ in a cavity, phononic waveguides coupled to an optical nanocavity⁶⁰, multiple levitated particles coupled to a joint cavity field⁶¹, or high-frequency bulk-acoustic wave resonators⁶².

In conclusion, we employed in this work a versatile nano-optomechanical platform to engineer phononic networks threaded by artificial magnetic fields, demonstrating Aharonov-Bohm interference between multiple loops. We found that the relative handedness of neighboring loops greatly impacts their dynamics: Networks with loops that have their vorticity aligned along shared links (i.e., staggered fluxes in contiguous plaquettes) behave like their constituent loops, while those with opposing vorticities show richer, flux-dependent, localization. Specifically, in the W_5 network, we uncovered a chiral edge mode that can be associated with topologically protected edge states in lattices with broken \mathcal{T} -symmetry. This minimal

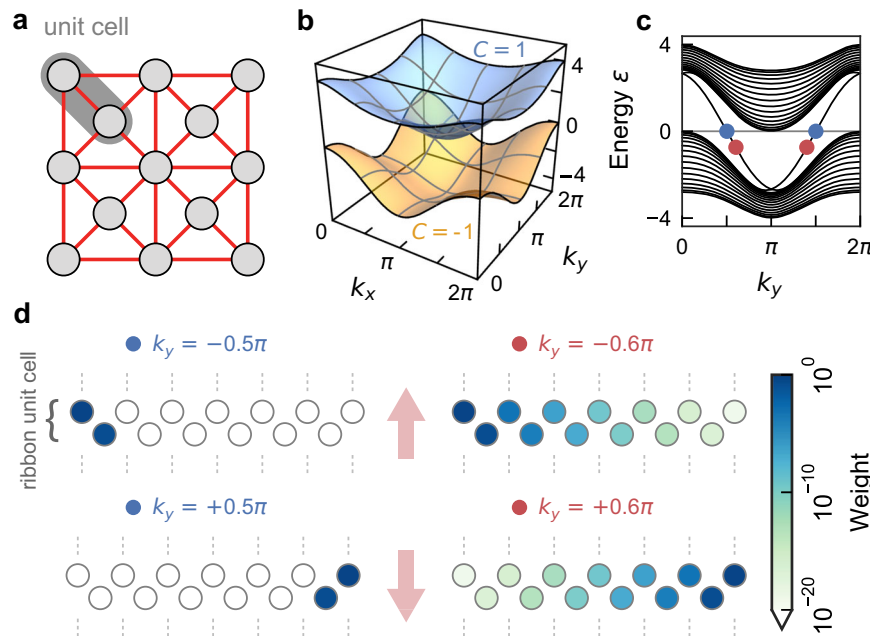


Fig. 5 | Example of extension to a large lattice: Union Jack lattice. **a** Square tiling of the W_5 network forms a Union Jack (UJ) lattice, featuring a two-site primitive unit cell (gray). **b** Two-dimensional band structure of a Union Jack lattice pierced by flux $\Phi = \pi/2$. Two bands with opposite Chern numbers $C = \pm 1$ are identified, separated by a gap. **c** Band structure of a UJ ribbon, finite in the x -direction (width $N = 33$ sites) and infinite in y . Two edge states traverse the topological gap, localized on either

boundary of the ribbon. **d** Transverse edge state profiles in a unit cell of the UJ ribbon, at different values of k_y , indicated by the colored dots in panel **c**. The panels show a single unit cell of the ribbon, which is extended to the top and bottom. The states are localized at one edge of the ribbon, depending on propagation direction. The transverse decay length depends on k_y . For $k_y = \pm \pi/2$, edge states fully localize on the outer two sites.

demonstration of a nanomechanical IQHE marks an essential step in the realization of Chern insulators for sound at the nanoscale⁹, and complements other experiments that achieve helical, bidirectional edge modes without breaking time-reversal symmetry³⁸.

The platform and mechanisms we demonstrate open a wealth of new directions for exploring how symmetry breaking and topology influence functionality and performance metrics of resonator networks, including sensing, thermodynamics, signal routing, and information processing. While we focus on IQHE physics here, the complete network programmability illustrated in this work allows programming various different phases of matter. In particular, the laser-controlled couplings will allow studying the physics of media and materials with time-varying Hamiltonians. The demonstrated optomechanical Aharonov-Bohm control could enable nanoscale devices with slow sound or phononic localization, enhancing energy-efficient control and acoustic sensing through flat band engineering and enhanced sound-matter interactions^{63,64}. Furthermore, this platform's weak, tunable nonlinearities from optomechanical interactions, combined with controllable connectivity, offer potential for analog computing, including Ising optimizers⁶⁵ and neuromorphic computers⁶⁶. Finally, the proposed principles could extend to hybrid quantum nanomechanical systems⁶⁷, where qubit-induced strong nonlinearity and flat bands enable strongly correlated chiral states akin to those in superconducting cavity arrays^{68,69}.

Methods

Experimental methods

The experimental set-up and methods for fabricating and characterizing the nano-optomechanical device, calibrating the programmable interactions, phase referencing, read-out, and driving of the resonator networks are described in detail in refs. 35–37. We summarize them here for completeness.

Optomechanical system

The nano-optomechanical device used in this work is fabricated in-house and consists of a suspended, sliced silicon nanobeam that incorporates a photonic crystal cavity. The optical cavity mode is simultaneously coupled to several non-degenerate flexural modes of the sliced beam, with spatial profiles shown in Fig. 1b. Optical access to the cavity is achieved via free-space coupling by focusing a laser beam at normal incidence onto the sample. To suppress direct reflections while collecting light escaping the cavity, we employ a cross-polarized detection configuration. The device is mounted in a room-temperature vacuum chamber (pressure 2×10^{-6} mbar) and aligned to the laser focus with a piezo-actuated precision stage. Supplementary Table 1 lists the relevant parameters of the five nanomechanical modes and the optical mode used in this study, determined as described in ref. 35.

Optically-mediated mechanical interactions

Direct mechanical coupling between the flexural modes is negligible due to their large frequency separation and narrow linewidths. However, effective interactions can be engineered via radiation pressure^{35–37}. In particular, intensity modulation of the laser drive provides parametric control of the cross-resonator optical spring effect, which, if the modulation matches the frequency difference between two resonators a_j and a_k , induces an effective beam-splitter interaction with rate

$$J_{jk} = c_{jk}^m \bar{n}_c \frac{g_{0,j} g_{0,k} \Delta}{\Delta^2 + \kappa^2/4} = c_{jk}^m \frac{\sqrt{\delta\omega_j \delta\omega_k}}{2}, \quad (7)$$

between a_j and a_k . Here, c_{jk}^m is the modulation depth, \bar{n}_c the average laser-induced cavity photon population, $g_{0,j}$ the vacuum optomechanical coupling rate of resonator j , $\Delta = \omega_L - \omega_c$ the detuning between the laser frequency ω_L and the cavity resonance ω_c , and κ the cavity

linewidth. Moreover, the coupling phase ϕ_{jk} is crucially controlled by the phase offset of the modulation tone.

Alternatively, J_{jk} can be succinctly expressed in terms of each resonator's optical spring shift $\delta\omega_j = 2\bar{n}_c g_{0,j}^2 \Delta / (\Delta^2 + \kappa^2/4)$. For a given optical input power, $\delta\omega_j$ and thus J_{jk} are maximized by detuning the control laser (Toptica CTL 1500) to the flank $\Delta = \pm \kappa / (2\sqrt{3})$ of the optical resonance. To calibrate the interaction strengths J_{jk} , we note that the spring shift $\delta\omega_j$ for each resonator j can be easily and accurately measured.

As mentioned in the main text, multiple modulation tones can be superimposed to induce several beam-splitter couplings at the same time. In experiment, modulation tones are generated by a high-frequency lock-in amplifier (LIA; Zurich Instruments UHFLI) supplemented by several additional signal generators (Siglent SDG1062X and SDG2122X). To achieve phase coherence between all tones, the signal generator clocks are synchronized to the LIA³⁷. After amplification, control signals are imprinted on the control laser field using a fiber-coupled intensity modulator (Thorlabs LN81S-FC).

Excitation and readout

The instantaneous displacement $z_j(t)$ of each mechanical resonator is transduced onto the reflected intensity of light from a secondary laser (Toptica CTL 1550), far detuned from the cavity resonance ($\Delta_{\text{det}} = -2.5\kappa$). This light is spectrally isolated from reflected control laser light by a tunable band-pass filter (DiCon) and detected by a fast, AC-coupled photodiode (New Focus 1811).

To extract individual resonator signals, the photodiode output is demodulated in the LIA with a 3 dB-bandwidth of 50 kHz (third order filter). The resulting complex amplitudes are then normalized to the detector voltage level corresponding to each resonator's zero-point motion x_{zpf} , as obtained from thermally driven reference measurements without coupling modulations. Under thermal driving, spectral analysis of the demodulated amplitude fluctuations then yields the thermomechanical spectra shown.

For the coherent response measurements shown in Fig. 4, we imprint a LIA-generated modulation resonant with a particular mechanical mode on the control laser intensity, in addition to the coupling tones that form the network. The response amplitudes of all resonators are analysed coherently by the LIA with a lock-in bandwidth of 10 Hz. Each data point in Fig. 4 is the average of 10 repetitions.

Analysis of the diamond network

In this section, we include further analysis of the diamond network shown in Fig. 2. First, we show that the dynamics of the chirality-opposed diamond (which has aligned vorticity along the central link), dubbed $\uparrow\downarrow, \diamond$ and shown in Fig. 2a, top, can be mapped onto the three-mode AB loop. The coupling matrix of a three-mode loop with one phase-carrying link of strength J_a and two reciprocal links of equal strength J_b is given by

$$\mathbf{J}_3 = \begin{bmatrix} 0 & J_a e^{-i\Phi} & J_b \\ J_a e^{i\Phi} & 0 & J_b \\ J_b & J_b & 0 \end{bmatrix}, \quad (8)$$

where Φ is the flux that pierces the loop. Next, we express the matrix $\mathbf{J}_{\uparrow\downarrow, \diamond}$ of the chirality-opposed diamond in the basis $\{\tilde{a}_{\text{apex}}, a_2, a_3, \tilde{a}_{\text{sym}}\}$, where $\tilde{a}_{\text{sym}} = (a_1 + a_2)/\sqrt{2}$ is the symmetric apex mode, to find

$$\mathbf{J}'_{\uparrow\downarrow, \diamond} = \begin{bmatrix} 0 & 0 & 0 & 0 \\ 0 & 0 & J_c e^{-i\Phi} & J\sqrt{2} \\ 0 & J_c e^{i\Phi} & 0 & J\sqrt{2} \\ 0 & J\sqrt{2} & J\sqrt{2} & 0 \end{bmatrix} = \begin{bmatrix} 0 & & & \\ & & & \\ & & & \mathbf{J}_3 \end{bmatrix}. \quad (9)$$

From Eq. (9), we see that the antisymmetric apex mode \tilde{a}_{apex} is decoupled, while the remaining modes $\{a_2, a_3, \tilde{a}_{\text{sym}}\}$ evolve as a three-

mode AB loop with couplings $J_a \rightarrow J_c, J_b \rightarrow J\sqrt{2}$. Moreover, when $J_c = J\sqrt{2}$, the effective three-mode loop exhibits equal couplings and is rotationally invariant.

For the equal-handed–vorticity-opposed– diamond shown in Fig. 2a, bottom, we calculate the spectra and eigenmodes for a range of central link strengths J_c . The results are shown in Supplementary Fig. 2. For $J_c = 0$, we recover the spectrum of the four-mode AB-loop defined by the diamond perimeter, with all eigenmodes completely delocalized. As discussed in the main text, the introduction of a coupling $J_c > 0$ along the central link couples the loop modes of opposite momenta $\tilde{a}_0 \leftrightarrow \tilde{a}_2$ and $\tilde{a}_1 \leftrightarrow \tilde{a}_{-1}$. These become degenerate for $\Phi = 0$ and $\Phi = \pi$, respectively. Consequently, a spectral gap opens at these fluxes. The associated (anti)symmetric superpositions of momentum states fully localize either in the apex or the central resonators.

Analysis of the W_5 wheel graph

In this section, we include further analysis of the W_5 wheel graph network, shown in Figs. 3 and 4. We map the dynamics of the opposite-chirality wheel graph in Fig. 3a, top, onto an effective three-mode AB loop. This network is dubbed $\uparrow\downarrow, \boxtimes$. First, we note that the W_5 network can be seen as a fusion of two vorticity-aligned diamond networks. This suggests us to express the wheel graph's Hamiltonian matrix $\mathbf{J}_{\uparrow\downarrow, \boxtimes}$ in the basis $\{\tilde{a}_{2-4}, \tilde{a}_{3-5}, \tilde{a}_{2+4}, \tilde{a}_{3+5}, a_1\}$, where $\tilde{a}_{j\pm k} = (a_j \pm a_k)/\sqrt{2}$ are symmetric and antisymmetric superpositions of the perimeter resonators, to find

$$\mathbf{J}_{\uparrow\downarrow, \boxtimes} = \begin{bmatrix} 0 & 0 & 0 & 0 & 0 \\ 0 & 0 & 0 & 0 & 0 \\ 0 & 0 & 0 & 2J & J_s \sqrt{2} e^{-i\Phi} \\ 0 & 0 & 2J & 0 & J_s \sqrt{2} e^{i\Phi} \\ 0 & 0 & J_s \sqrt{2} e^{i\Phi} & J_s \sqrt{2} e^{-i\Phi} & 0 \end{bmatrix} = \begin{bmatrix} 0 & & & & \\ & 0 & & & \\ & & & & \\ & & & & \mathbf{J}_3 \end{bmatrix}. \quad (10)$$

Similar to the apex mode in the diamond, the two antisymmetric perimeter modes $\tilde{a}_{2-4}, \tilde{a}_{3-5}$ are decoupled. The remaining modes evolve under the Hamiltonian \mathbf{J}'_3 of a three-mode AB loop with couplings $J_a \rightarrow 2J, J_b \rightarrow J_s \sqrt{2}$, pierced by a net flux of $\Phi \rightarrow 2\Phi$ that is distributed evenly over the last two links.

Independent prediction of W_5 response

In the homogeneous W_5 network, we predict the response to coherent driving, as shown in Fig. 4a, from the network's susceptibility matrix

$$\chi_{\vec{a}} \rightarrow (\Delta_m) = i(\Delta_m \mathbb{1} - \mathbf{J} + i\mathbf{\Gamma}/2)^{-1}. \quad (11)$$

Each resonator j can be driven individually, through radiation pressure, by modulating the intensity of a weak drive laser with a coherent tone at a frequency $\omega_{d,j}$ close the mechanical resonance frequency Ω_j . In Eq. (11), $\Delta_m = \omega_{d,j} - \Omega_j$ is the global detuning of all driving tones, while

$$\mathbf{J} = \begin{bmatrix} 0 & J_s & J_s & J_s & J_s \\ J_s & 0 & J e^{-i\Phi} & 0 & J e^{i\Phi} \\ J_s & J e^{i\Phi} & 0 & J e^{-i\Phi} & 0 \\ J_s & 0 & J e^{i\Phi} & 0 & J e^{-i\Phi} \\ J_s & J e^{-i\Phi} & 0 & J e^{i\Phi} & 0 \end{bmatrix} \quad (12)$$

is the network's Hamiltonian matrix and $\mathbf{\Gamma} = \text{diag}(\gamma_1, \dots, \gamma_N)$ encodes the mechanical dissipation rates γ_j , as listed in Supplementary Table I. In our experiment, the drive laser is resonant with the optical cavity.

The vector \vec{a} of the resonators' complex response amplitudes a_j , expressed in units of the zero-point motion $x_{\text{zpf},j}$ and in a frame that

rotates along with each resonator j , is then given by

$$\vec{\alpha} = \mathbf{X}_{\vec{\alpha}}(\Delta_m)\vec{f}. \quad (13)$$

Each element of \vec{f} encodes the complex amplitude

$$f_j = ie^{i\phi_{a,j}} c_{d,j} \frac{g_{0,j}\bar{n}_d}{2} \quad (14)$$

of the tone driving resonator j with modulation depth $c_{d,j}$, phase offset $\phi_{d,j}$ and corresponding optomechanical coupling rate $g_{0,j}$, while \bar{n}_d denotes the average cavity photon population contributed by the weak, resonant drive laser.

Drive and response amplitudes are normalized such that

$$\alpha_j = f_j / (y_j/2 - i\Delta_m) \quad (15)$$

when all resonators are uncoupled ($\mathbf{J} = \mathbf{0}$). In practice, we establish the value of the proportionality constant $d_j = g_{0,j}\bar{n}_d/2$ between $|f_j|$ and $c_{d,j}$ in a calibration experiment where, for each resonator j individually, we measure α_j as a function of Δ_m for fixed $c_{d,j}$. We then fit Eq. (15) to the results to extract d_j . For the experiments shown in Fig. 4a, we used driving strengths $f_j/(2\pi) = 1.91$ MHz (left) and $f_j/(2\pi) = 2.07$ MHz (middle and right).

Topology of the W_5 lattice

In the main text, we have explored W_5 graphs threaded by synthetic fluxes. By concatenating these W_5 building blocks, one can construct the Union Jack (UJ) lattice, where each W_5 graph forms the fundamental unit (Supplementary Fig. 5a). This lattice is generated by subdividing the squares of a standard square lattice into triangles, with the diagonals and edges naturally forming the connections of the W_5 structure. Within the W_5 lattice, the sites can be distinguished into two sublattices based on their roles and connectivity. The central or ‘‘hub’’ sites of the W_5 graphs form one sublattice and link directly to the four surrounding peripheral or ‘‘rim’’ sites. The peripheral sites, which belong to the second sublattice, form a closed loop and are shared between neighboring W_5 units.

In the simulations, the Union Jack lattice is constructed by first defining a basis with two sites: one site a at the origin $(0, 0)$ and another site b at $(\ell/2, \ell/2)$ – the site to become a hub. The primitive vectors of the lattice are then chosen as $\vec{\ell}_1 = (\ell, 0)$ and $\vec{\ell}_2 = (0, \ell)$, which define a square unit cell of side length ℓ . We label each unit cell by its position indices j and k along the lattice vectors $j\vec{\ell}_1 + k\vec{\ell}_2$. The standard nearest-neighbor connections between the sites $a_{j,k}$ at the corners of the squares form the perimetral structure of the lattice. Diagonal connections are then added between each of these corner sites and the central site $b_{j,k}$ in the same and neighboring unit cells, creating the characteristic structure of the UJ lattice.

Hofstadter butterfly spectra

The Hofstadter butterfly spectrum describes the energy spectrum of excitations on a 2D periodic lattice subject to a synthetic flux per plaquette, $\Phi = 2\pi p/q$, where p and q are coprime integers. The spectrum, plotted as a function of Φ , reveals a fractal pattern of gaps and bands resulting from the interplay between the geometric length, $l_g - \ell$, set by the lattice spacing, and the magnetic length, $l_\Phi \sim 1/\sqrt{\Phi}$, which characterizes the spatial extent of the synthetic flux’s influence. In the square lattice, when Φ is rational, l_g and l_Φ commensurate, splitting each energy band into q magnetic subbands and producing the fractal Hofstadter butterfly⁴³, as shown in Supplementary Fig. 6a.

For the triangular lattice, the Hofstadter butterfly appears more intricate. Each energy band splits into q magnetic subbands when $\Phi = 2\pi p/q$ ^{53,70}, Supplementary Fig. 6b. The shorter path connectivity of

the triangular lattice distorts the fractal symmetry and modifies the gap structure compared to the square lattice, resulting in a richer but less symmetric spectrum. For the Union Jack lattice, shown in Supplementary Fig. 6c, the Hofstadter butterfly spectrum combines features of both the square and triangular lattices. The hybrid connectivity of the Union Jack lattice creates a unique energy spectrum where the fractal structure of the Hofstadter butterfly still emerges, but with distinct gap patterns and subband structures characteristic of its geometry. This spectrum reflects the influence of both square-like perimetral bonds and the central hub connections, highlighting the interplay of the lattice’s hybrid nature with the magnetic flux.

Band structure of the UJ lattice with $\Phi = \pi/2$

For a planar UJ lattice with translational invariance in both directions, where each triangular plaquette is pierced by a homogeneous flux $\Phi = \pi/2$, the magnetic unit cell (Supplementary Fig. 5b) is equal to the lattice unit cell. The Hamiltonian H that governs the lattice is specified by the matrix elements

$$\begin{aligned} \langle a_{j,k} | H | a_{j+1,k} \rangle &= J, & \langle a_{j,k} | H | a_{j,k+1} \rangle &= J, \\ \langle a_{j,k} | H | b_{j,k} \rangle &= -J, & \langle b_{j,k} | H | a_{j+1,k+1} \rangle &= J, \\ \langle b_{j,k} | H | a_{j,k+1} \rangle &= -iJ, & \langle a_{j+1,k} | H | b_{j,k} \rangle &= -iJ, \end{aligned} \quad (16)$$

and their Hermitian conjugates. These elements encode the couplings within and between unit cells as shown in Supplementary Fig. 5b by solid links, where J is the coupling strength.

To calculate the band structure of this infinite, two-dimensional lattice, we take the dynamical matrix of the magnetic unit cell and apply the Bloch theorem for periodic boundary conditions,

$$\langle (a, b)_{j+n, k+m} \rangle = e^{i(nk_x + mk_y)} \langle (a, b)_{j,k} \rangle, \quad (17)$$

for wavevectors k_x and k_y in the x and y -directions, respectively. The matrix elements of H that drive rim site $a_{j,k}$ correspond to all links that connect to the a -site in Supplementary Fig. 5b (solid and dashed), and are given by

$$\begin{aligned} \langle a_{j,k} | H | a_{j+1,k} \rangle &= J, & \langle a_{j,k} | H | a_{j,k+1} \rangle &= J, \\ \langle a_{j,k} | H | a_{j-1,k} \rangle &= J, & \langle a_{j,k} | H | a_{j,k-1} \rangle &= J, \\ \langle a_{j,k} | H | b_{j,k} \rangle &= -J, & \langle a_{j,k} | H | b_{j-1,k} \rangle &= -iJ, \\ \langle a_{j,k} | H | b_{j-1,k-1} \rangle &= J, & \langle a_{j,k} | H | b_{j,k-1} \rangle &= iJ. \end{aligned} \quad (18)$$

Likewise, the matrix elements that drive hub site $b_{j,k}$ are given by

$$\begin{aligned} \langle b_{j,k} | H | a_{j,k} \rangle &= -J, & \langle b_{j,k} | H | a_{j+1,k} \rangle &= iJ, \\ \langle b_{j,k} | H | a_{j,k+1} \rangle &= -iJ, & \langle b_{j,k} | H | a_{j+1,k+1} \rangle &= J. \end{aligned} \quad (19)$$

By combining Eqs. (18) and (19) with boundary condition (17), we arrive at the 2×2 Bloch Hamiltonian H_B for the unit cell sites a and b , specified by matrix elements

$$\begin{aligned} \langle a | H_B | a \rangle &= J(e^{-ik_x} + e^{ik_x} + e^{-ik_y} + e^{ik_y}) \\ \langle a | H_B | b \rangle &= J(e^{-i(k_x + k_y)} - 1 - ie^{-ik_x} + ie^{-ik_y}), \\ \langle b | H_B | a \rangle &= J(e^{i(k_x + k_y)} - 1 + ie^{ik_x} - ie^{ik_y}), \\ \langle b | H_B | b \rangle &= 0. \end{aligned}$$

The band structure of H_B is given by its two eigenvalues

$$\frac{\epsilon_{\pm}}{J} = \cos(k_x) + \cos(k_y) \pm \sqrt{4 + (\cos(k_x) - \cos(k_y))^2}, \quad (20)$$

which are plotted in Fig. 5b.

Chern numbers for flux $\Phi = \pi/2$

We study the integer quantum Hall effect, a well-known topological phase of matter, in this UJ lattice. Topological phases exhibit properties that are robust against local perturbations, with quantized conductance values tied to global invariants in condensed-matter systems. In this case, the quantized Hall conductance is linked to the topology of the system's electronic bands, described by the Chern number. Similar concepts extend to topological bosonics, e.g., topological photonics, where the Chern number governs robust light transport, enabling unidirectional edge states immune to backscattering⁸.

Starting from the Bloch eigenstates $|u_{\pm}(\vec{k})\rangle$ corresponding to the two eigenvalues ϵ_{\pm} of H_B , the Berry curvature Ω_{\pm} is calculated for each band as

$$\Omega_{\pm}(\vec{k}) = 2 \operatorname{Im} \left\langle \partial_{k_x} u_{\pm}(\vec{k}) \left| \partial_{k_y} u_{\pm}(\vec{k}) \right. \right\rangle, \quad (21)$$

having only one component in 2D. The Berry curvature acts as a momentum-space curvature, and its integral reveals the topological nature of the band. The net flux of Berry curvature over the Brillouin zone (BZ) gives the Chern number:

$$C_{\pm} = \frac{1}{2\pi} \int_{\text{BZ}} d\vec{k} \Omega_{\pm}(\vec{k}). \quad (22)$$

This invariant reflects the global structure of the band in a manner analogous to the Gauss-Bonnet theorem, where the integral of Gaussian curvature encodes a topological property (the Euler characteristic) of a surface⁷¹. We calculate the Chern numbers for the UJ lattice symbolically, using MATHEMATICA software, and find

$$C_{\pm} = \pm 1. \quad (23)$$

This result indicates that the UJ lattice hosts topologically nontrivial phases, with $C_+ = 1$ and $C_- = -1$ corresponding to chiral edge states propagating in opposite directions, as per the bulk-boundary correspondence.

Direct retrieval of edge states

A ribbon geometry imposes translational symmetry along the y -direction (infinite) while keeping the network finite in the x -direction to form a ribbon of fixed width N . This setup isolates edge states, allowing the study of chiral modes induced by the flux Φ .

A natural gauge choice for the ribbon is the Landau gauge, where link phases vary only in the x -direction. In Supplementary Fig. 5c, we show how the UJ lattice can be constructed with arbitrary flux Φ in this gauge. The ribbon consists of a single row of N primitive unit cells, labeled by their index j along the x -direction, and comprises the sites a_j and b_j . To ensure termination on a rim site on both ends, we remove the final hub site b_N .

To calculate the band structure of the infinite ribbon (as plotted in Fig. 5c) and the corresponding eigenstates (as plotted in Fig. 5d), we construct the Bloch Hamiltonian H_B in a similar fashion as before. We find that it is specified by the matrix elements

$$\begin{aligned} \langle a_j | H_B | a_j \rangle &= 2J \cos(k_y - 4j\Phi), \\ \langle a_j | H_B | b_j \rangle &= J \left(e^{2i\Phi} + e^{-ik_y} e^{-i(3+4j)\Phi} \right), \\ \langle b_j | H_B | a_j \rangle &= J \left(e^{-2i\Phi} + e^{ik_y} e^{i(3+4j)\Phi} \right), \end{aligned} \quad (24)$$

that couple sites within a cell j , and the inter-cell matrix elements

$$\begin{aligned} \langle a_j | H_B | a_{j+1} \rangle &= J, \\ \langle a_{j+1} | H_B | a_j \rangle &= J, \\ \langle b_j | H_B | a_{j+1} \rangle &= J \left(e^{-3i\Phi} + e^{ik_y} e^{i(4+4j)\Phi} \right), \\ \langle a_{j+1} | H_B | b_j \rangle &= J \left(e^{3i\Phi} + e^{-ik_y} e^{-i(4+4j)\Phi} \right), \end{aligned} \quad (25)$$

while all other elements are zero. Again, the eigenvalues of H_B determine the dispersion of the ribbon, while the corresponding eigenvectors determine its wave states.

Data availability

The data in this study are available from the Zenodo repository at <https://doi.org/10.5281/zenodo.16001393>.

References

1. v. Klitzing, K., Dorda, G. & Pepper, M. New method for high-accuracy determination of the fine-structure constant based on quantized Hall resistance. *Phys. Rev. Lett.* **45**, 494–497 (1980).
2. Thouless, D. J., Kohmoto, M., Nightingale, M. P. & den Nijs, M. Quantized Hall conductance in a two-dimensional periodic potential. *Phys. Rev. Lett.* **49**, 405–408 (1982).
3. Cohen, E. et al. Geometric phase from Aharonov–Bohm to Pancharatnam–Berry and beyond. *Nat. Rev. Phys.* **1**, 437–449 (2019).
4. Hasan, M. Z. & Kane, C. L. *Colloquium: topological insulators*. *Rev. Mod. Phys.* **82**, 3045–3067 (2010).
5. Laughlin, R. B. Quantized Hall conductivity in two dimensions. *Phys. Rev. B* **23**, 5632–5633 (1981).
6. Haldane, F. D. M. & Raghu, S. Possible realization of directional optical waveguides in photonic crystals with broken time-reversal symmetry. *Phys. Rev. Lett.* **100**, 013904 (2008).
7. Raghu, S. & Haldane, F. D. M. Analogs of quantum-hall-effect edge states in photonic crystals. *Phys. Rev. A* **78**, 033834 (2008).
8. Ozawa, T. et al. Topological photonics. *Rev. Mod. Phys.* **91**, 015006 (2019).
9. Shah, T., Brendel, C., Peano, V. & Marquardt, F. *Colloquium: Topologically protected transport in engineered mechanical systems*. *Rev. Mod. Phys.* **96**, 021002 (2024).
10. Umucallilar, R. O. & Carusotto, I. Artificial gauge field for photons in coupled cavity arrays. *Phys. Rev. A* **84**, 043804 (2011).
11. Wang, Z., Chong, Y., Joannopoulos, J. D. & Soljačić, M. Observation of unidirectional backscattering-immune topological electromagnetic states. *Nature* **461**, 772–775 (2009).
12. Klembt, S. et al. Exciton-polariton topological insulator. *Nature* **562**, 552–556 (2018).
13. Fleury, R., Sounas, D. L., Sieck, C. F., Haberman, M. R. & Alù, A. Sound isolation and giant linear nonreciprocity in a compact acoustic circulator. *Science* **343**, 516–519 (2014).
14. Nash, L. M. et al. Topological mechanics of gyroscopic metamaterials. *Proc. Natl. Acad. Sci. USA* **112**, 14495–14500 (2015).
15. Koch, J., Houck, A. A., Hur, K. L. & Girvin, S. M. Time-reversal-symmetry breaking in circuit-QED-based photon lattices. *Phys. Rev. A* **82**, 043811 (2010).
16. Nunnenkamp, A., Koch, J. & Girvin, S. M. Synthetic gauge fields and homodyne transmission in Jaynes–Cummings lattices. *N. J. Phys.* **13**, 095008 (2011).
17. Dalibard, J., Gerbier, F., Juzeliūnas, G. & Öhberg, P. *Colloquium: artificial gauge potentials for neutral atoms*. *Rev. Mod. Phys.* **83**, 1523–1543 (2011).
18. Fang, K., Yu, Z. & Fan, S. Photonic Aharonov–Bohm effect based on dynamic modulation. *Phys. Rev. Lett.* **108**, 153901 (2012).
19. Sounas, D. L. & Alù, A. Non-reciprocal photonics based on time modulation. *Nat. Photon.* **11**, 774–783 (2017).

20. Darabi, A., Ni, X., Leamy, M. & Alù, A. Reconfigurable Floquet elastodynamic topological insulator based on synthetic angular momentum bias. *Sci. Adv.* **6**, eaba8656 (2020).
21. Aidelburger, M. et al. Experimental realization of strong effective magnetic fields in an optical lattice. *Phys. Rev. Lett.* **107**, 255301 (2011).
22. Aidelburger, M., Nascimbene, S. & Goldman, N. Artificial gauge fields in materials and engineered systems. *C. R. Phys.* **19**, 394–432 (2018).
23. Fang, K., Yu, Z. & Fan, S. Realizing effective magnetic field for photons by controlling the phase of dynamic modulation. *Nat. Photon.* **6**, 782–787 (2012).
24. Goldman, N., Budich, J. C. & Zoller, P. Topological quantum matter with ultracold gases in optical lattices. *Nat. Phys.* **12**, 639–645 (2016).
25. Ningyuan, J., Owens, C., Sommer, A., Schuster, D. & Simon, J. Time- and site-resolved dynamics in a topological circuit. *Phys. Rev. X* **5**, 021031 (2015).
26. Ruesink, F., Miri, M.-A., Alù, A. & Verhagen, E. Nonreciprocity and magnetic-free isolation based on optomechanical interactions. *Nat. Commun.* **7**, 13662 (2016).
27. Fang, K. et al. Generalized non-reciprocity in an optomechanical circuit via synthetic magnetism and reservoir engineering. *Nat. Phys.* **13**, 465–471 (2017).
28. Bernier, N. R. et al. Nonreciprocal reconfigurable microwave optomechanical circuit. *Nat. Commun.* **8**, 604 (2017).
29. Peterson, G. A. et al. Demonstration of efficient nonreciprocity in a microwave optomechanical circuit. *Phys. Rev. X* **7**, 031001 (2017).
30. Verhagen, E. & Alù, A. Optomechanical nonreciprocity. *Nat. Phys.* **13**, 922–924 (2017).
31. Xu, H., Jiang, L., Clerck, A. A. & Harris, J. G. E. Nonreciprocal control and cooling of phonon modes in an optomechanical system. *Nature* **568**, 65–69 (2019).
32. Mathew, J. P., del Pino, J. & Verhagen, E. Synthetic gauge fields for phonon transport in a nano-optomechanical system. *Nat. Nanotechnol.* **15**, 198–202 (2020).
33. Peano, V., Brendel, C., Schmidt, M. & Marquardt, F. Topological phases of sound and light. *Phys. Rev. X* **5**, 031011 (2015).
34. Schmidt, M., Kessler, S., Peano, V., Painter, O. & Marquardt, F. Optomechanical creation of magnetic fields for photons on a lattice. *Optica* **2**, 635 (2015).
35. del Pino, J., Slim, J. J. & Verhagen, E. Non-Hermitian chiral phonics through optomechanically induced squeezing. *Nature* **606**, 82–87 (2022).
36. Wanjura, C. C. et al. Quadrature nonreciprocity in bosonic networks without breaking time-reversal symmetry. *Nat. Phys.* **19**, 1429–1436 (2023).
37. Slim, J. J. et al. Optomechanical realization of the bosonic Kitaev chain. *Nature* **627**, 767–771 (2024).
38. Ren, H. et al. Topological phonon transport in an optomechanical system. *Nat. Commun.* **13**, 3476 (2022).
39. Youssefi, A. et al. Topological lattices realized in superconducting circuit optomechanics. *Nature* **612**, 666–672 (2022).
40. Leijssen, R. & Verhagen, E. Strong optomechanical interactions in a sliced photonic crystal nanobeam. *Sci. Rep.* **5**, 15974 (2015).
41. Chartrand, G. *Introductory graph theory* (Courier Corporation, 2012).
42. Kemmerly, J. E. & Hayt, W. *Engineering circuit analysis* (McGraw-Hill, 1993).
43. Hofstadter, D. R. Energy levels and wave functions of Bloch electrons in rational and irrational magnetic fields. *Phys. Rev. B* **14**, 2239–2249 (1976).
44. Aoki, H., Ando, M. & Matsumura, H. Hofstadter butterflies for flat bands. *Phys. Rev. B* **54**, R17296–R17299 (1996).
45. Vidal, J., Mosseri, R. & Douçot, B. Aharonov-Bohm cages in two-dimensional structures. *Phys. Rev. Lett.* **81**, 5888–5891 (1998).
46. Leykam, D., Andreev, A. & Flach, S. Artificial flat band systems: From lattice models to experiments. *Adv. Phys. X* **3**, 1473052 (2018).
47. Mukherjee, S., Di Liberto, M., Öhberg, P., Thomson, R. R. & Goldman, N. Experimental observation of Aharonov-Bohm cages in photonic lattices. *Phys. Rev. Lett.* **121**, 075502 (2018).
48. Tang, L. et al. Photonic flat-band lattices and unconventional light localization. *Nanophotonics* **9**, 1161–1176 (2020).
49. Kremer, M. et al. A square-root topological insulator with non-quantized indices realized with photonic Aharonov-Bohm cages. *Nat. Commun.* **11**, 907 (2020).
50. Gumbs, G. & Fekete, P. Hofstadter butterfly for the hexagonal lattice. *Phys. Rev. B Condens. Matter Mater. Phys.* **56**, 3787–3791 (1997).
51. Avron, J., Kenneth, O. & Yehoshua, G. A study of the ambiguity in the solutions to the diophantine equation for Chern numbers. *J. Phys. A: Math. Theor.* **47**, 185202 (2014).
52. Agazzi, A., Eckmann, J. P. & Graf, G. M. The colored Hofstadter butterfly for the honeycomb lattice. *J. Stat. Phys.* **156**, 417–426 (2014).
53. Du, L., Chen, Q., Barr, A. D., Barr, A. R. & Fiete, G. A. Floquet Hofstadter butterfly on the kagome and triangular lattices. *Phys. Rev. B* **98**, 1–12 (2018).
54. Stegmaier, A., Upreti, L. K., Thomale, R. & Boettcher, I. Universality of Hofstadter butterflies on hyperbolic lattices. *Phys. Rev. Lett.* **128**, 166402 (2022).
55. Stephenson, J. Ising model with antiferromagnetic next-nearest-neighbor coupling: spin correlations and disorder points. *Phys. Rev. B* **1**, 4405–4409 (1970).
56. Grünbaum, B. & Shephard, G. C. *Tilings and Patterns* (W.H. Freeman, New York, 1987).
57. Leijssen, R., La Gala, G. R., Freisem, L., Muhonen, J. T. & Verhagen, E. Nonlinear cavity optomechanics with nanomechanical thermal fluctuations. *Nat. Commun.* **8**, 16024 (2017).
58. Aspelmeyer, M., Kippenberg, T. J. & Marquardt, F. Cavity optomechanics. *Rev. Mod. Phys.* **86**, 1391–1452 (2014).
59. Hälgl, D. et al. Strong parametric coupling between two ultra-coherent membrane modes. *Phys. Rev. Lett.* **128**, 094301 (2022).
60. Patel, R. N. et al. Single-mode phononic wire. *Phys. Rev. Lett.* **121**, 040501 (2018).
61. Rieser, J. et al. Tunable light-induced dipole-dipole interaction between optically levitated nanoparticles. *Science* **377**, 987–990 (2022).
62. Kharel, P. et al. High-frequency cavity optomechanics using bulk acoustic phonons. *Sci. Adv.* **5**, eaav0582 (2019).
63. Yang, Z. et al. Topological acoustics. *Phys. Rev. Lett.* **114**, 1–4 (2015).
64. Ma, T.-X., Fan, Q.-S., Zhang, C. & Wang, Y.-S. Acoustic flatbands in phononic crystal defect lattices. *J. Appl. Phys.* **129**, 145104 (2021).
65. Mahboob, I., Okamoto, H. & Yamaguchi, H. An electromechanical Ising Hamiltonian. *Sci. Adv.* **2**, e1600236 (2016).
66. Marković, D., Mizrahi, A., Querlioz, D. & Grollier, J. Physics for neuromorphic computing. *Nat. Rev. Phys.* **2**, 499–510 (2020).
67. Chu, Y. et al. Quantum acoustics with superconducting qubits. *Science* **358**, 199–202 (2017).
68. Roushan, P. et al. Chiral ground-state currents of interacting photons in a synthetic magnetic field. *Nat. Phys.* **13**, 146–151 (2017).
69. Rosen, I. T. et al. A synthetic magnetic vector potential in a 2d superconducting qubit array. *Nat. Phys.* **20**, 1881–1887 (2024).
70. Hasegawa, Y., Lederer, P., Rice, T. M. & Wiegmann, P. B. Theory of electronic diamagnetism in two-dimensional lattices. *Phys. Rev. Lett.* **63**, 907–910 (1989).
71. Do Carmo, M. P. *Differential geometry of curves and surfaces: revised and updated second edition* (Courier Dover Publications, 2016).

Acknowledgements

This work is part of the research program of the Netherlands Organisation for Scientific Research. It is funded by the European Union, supported by ERC Grants 759644 (TOPP) and 101088055 (Q-MEME). Views and opinions expressed are however those of the authors only and do not necessarily reflect those of the European Union or the European Research Council Executive Agency. Neither the European Union nor the granting authority can be held responsible for them. J.J.S. acknowledges support from the Australian Research Council Centre of Excellence for Engineered Quantum Systems (EQUS, CE170100009). J.d.P. acknowledges financial support from the ETH Fellowship program (Grant No. 20-2 FEL-66).

Author contributions

E.V. conceived the project, and all authors designed the experiments together. J.J.S. fabricated the sample, developed the experimental methods, performed the experiments, and analysed the data. J.d.P. and J.J.S. developed the theory. All authors contributed to the interpretation of the results and writing the manuscript. E.V. supervised the work.

Competing interests

The authors declare no competing interests.

Additional information

Supplementary information The online version contains supplementary material available at <https://doi.org/10.1038/s41467-025-62541-z>.

Correspondence and requests for materials should be addressed to Ewold Verhagen.

Peer review information *Nature Communications* thanks Yu-Gui Peng and the other anonymous reviewers for their contribution to the peer review of this work. A peer review file is available.

Reprints and permissions information is available at <http://www.nature.com/reprints>

Publisher's note Springer Nature remains neutral with regard to jurisdictional claims in published maps and institutional affiliations.

Open Access This article is licensed under a Creative Commons Attribution-NonCommercial-NoDerivatives 4.0 International License, which permits any non-commercial use, sharing, distribution and reproduction in any medium or format, as long as you give appropriate credit to the original author(s) and the source, provide a link to the Creative Commons licence, and indicate if you modified the licensed material. You do not have permission under this licence to share adapted material derived from this article or parts of it. The images or other third party material in this article are included in the article's Creative Commons licence, unless indicated otherwise in a credit line to the material. If material is not included in the article's Creative Commons licence and your intended use is not permitted by statutory regulation or exceeds the permitted use, you will need to obtain permission directly from the copyright holder. To view a copy of this licence, visit <http://creativecommons.org/licenses/by-nc-nd/4.0/>.

© The Author(s) 2025